Article

Polyaniline-Derived Nitrogen-Containing Carbon Nanostructures with Different Morphologies as Anode Modifier in Microbial Fuel Cells

Irina Lascu [1], Claudiu Locovei [2,3], Corina Bradu [1], Cristina Gheorghiu [4], Ana Maria Tanase [1,*] and Anca Dumitru [2,*]

[1] Faculty of Biology, University of Bucharest, Splaiul Independenței 91–95, 050095 Bucharest, Romania
[2] Faculty of Physics, University of Bucharest, P.O. Box MG-11, 077125 Magurele, Romania
[3] National Institute of Materials Physics, Atomistilor 405A, 077125 Magurele, Romania
[4] Extreme Light Infrastructure-Nuclear Physics (ELI-NP), "Horia Hulubei" National Institute for R&D in Physics and Nuclear Engineering, P.O. Box MG-6, 077125 Magurele, Romania
* Correspondence: ana-maria.tanase@bio.unibuc.ro (A.M.T.); anka.dumitru@gmail.com (A.D.)

Abstract: Anode modification with carbon nanomaterials is an important strategy for the improvement of microbial fuel cell (MFC) performance. The presence of nitrogen in the carbon network, introduced as active nitrogen functional groups, is considered beneficial for anode modification. In this aim, nitrogen-containing carbon nanostructures (NCNs) with different morphologies were obtained via carbonization of polyaniline and were further investigated as anode modifiers in MFCs. The present study investigates the influence of NCN morphology on the changes in the anodic microbial community and MFC performance. Results show that the nanofibrillar morphology of NCNs is beneficial for the improvement of MFC performance, with a maximum power density of 40.4 mW/m², 1.25 times higher than the anode modified with carbonized polyaniline with granular morphology and 2.15 times higher than MFC using the carbon cloth-anode. The nanofibrillar morphology, due to the well-defined individual nanofibers separated by microgaps and micropores and a better organization of the carbon network, leads to a larger specific surface area and higher conductivity, which can allow more efficient substrate transport and better bacterial colonization with greater relative abundances of *Geobacter* and *Thermoanaerobacter*, justifying the improvement of MFC performance.

Keywords: microbial fuel cell; anode modification; polyaniline; carbonization; nitrogen-containing carbon nanostructures; biofilm; microbial diversity; extracellular electron transfer

1. Introduction

Bioelectrochemical systems (BES) represent different biofilm-based bioreactors that include microbial fuel cells (MFC), microbial electrolysis cells (MEC), microbial desalination cells (MDC), and microbial reverse electrodialysis cells (MRC) and hold great promise for sustainable production of energy and positive wastewater treatment [1–6]. Among them, microbial fuel cell (MFC) is an emerging technology that uses bacterial metabolism and electrochemical processes for both wastewater treatment and bioenergy production. MFC integrates bioelectrochemically active microorganism growth in the form of biofilms on the electrode surface to produce bioelectricity from a variety of organic substrates [1,7]. Anode materials, structure, and configuration, together with microbial biofilms colonizing anodic electrodes, are the key factors that affect the performance of MFCs [7–12]. The vital role of anode materials is given by their direct contact with bacteria, affecting bacterial attachments and the electron transfer rate from electrochemically active bacteria to the anode surface [13,14]. The main properties of the anode materials that can improve the MFC performance include electrical conductivity, chemical stability and durability,

biocompatibility, cost and accessibility. A wide variety of materials, such as conventional and advanced carbon materials, metal-based or metal composites, conducting polymers, and composite materials, have been used to enhance the performance of MFCs [9,14]. Among them, carbon-based electrodes have been extensively studied due to their chemical stability and high electrical conductivity, but the hydrophobic characteristic of their surface does not favor bacterial adhesion and, as a consequence, electron transfer capacity. Thus, the use of MFC anodes modified with nanomaterials seems to be a promising strategy for the improvement of MFCs performance compared with plain carbon anodes [7,9]. In this aim, anode modification with carbon nanostructures increases the surface area for the attachment of microorganisms, which favors the kinetics of electron transfer [9,14]. As well, the incorporation of heteroatoms in the graphitic network can enhance both the conductivity and the catalytic activity of the material, attracting great interest in energy and environmental applications [15–17]. As reported recently, the incorporation of heteroatoms into carbon can disturb the sp^2-hybridized graphitic network, interfering in charge distribution, and could tailor its electron-donor properties for required electrical and chemical performance, thus expanding the property of carbon materials [18,19]. To this extent, nitrogen-doped carbon nanostructures, such as nitrogen-doped ordered mesoporous carbon [20], N-doped carbon nanotube [21], nitrogen-doped graphene [22], self-nitrogen-doped carbon nanosheets [23], and nitrogen-doped carbon dots [24], were used for anode modification and show an improved MFC performance, which was attributed to the nitrogen functionality. Among various strategies that have been developed to introduce nitrogen functionality on the anode surface, direct annealing of N-containing precursors (i.e., polyaniline, polypyrrole, polydopamine) under an inert atmosphere [15,25–28] can simplify the preparation processes and reduce cost. Polyaniline (PANI), as a nitrogen-containing carbon precursor, has been widely investigated for electrochemical energy conversion and storage applications due to its easy synthesis, high environmental stability, low production cost, and high nitrogen content [19,27,28]. There are few studies that mention the use of carbonized PANI in BES [19,29–31]. Thus, carbonised PANI was used for the modification of a commercial sponge in order to improve the MFC performance [19], a graphene oxide-supported carbon nanofiber-like network derived from polyaniline was used as an anode in a glucose/O_2 fuel cell [29], a novel three-dimensional (3D) carbon composite of PANI$_{1600}$@CNTs was applied to enhance a enzymatic biofuel cell [30] and a 3D carbon foam with surface-anchored nitrogen-containing carbon nanoparticles derived from PANI as a freestanding anode in MFC [31].

Furthermore, the use of mixed microbial communities in MFCs (such as municipal wastewater, activated sludge and soil sediment) gained a lot of attention due to their stability and high power production compared with pure cultures [32,33]. Understanding the microbial consortium changes during the process would allow researchers to harness microbial functions to obtain more efficient electricity from MFCs.

In our study, we synthesized polyaniline with different morphologies, which were then used as precursors for nitrogen-containing carbon nanostructures (NCNs). The resulting NCNs with different morphology were used as anode modifiers in an MFC system loaded with municipal wastewater, and the microbial diversity of the resulting biofilms formed on the anode surface was analyzed, along with that of the initial wastewater, through high-throughput short read sequencing. The present study investigates how the changes in NCN morphology and anodic microbial community affect MFC performance, which, to our knowledge, has not been reported in the existing literature.

2. Results and Discussions

2.1. Characterization of Polymer Precursors and Corresponding Nitrogen-Containing Carbon Nanostructures

2.1.1. Surface Characterization and Elemental Composition by SEM/EDX

Two different synthesis methods used in our work allowed for the synthesis of polyaniline with different morphologies, one with near-granular-shaped nanoparticles (PANI-R) and another with nanofibrillar morphology (PANI-T). Direct carbonization of polymeric precursors (PANI-R and PANI-T) allowed us to obtain NCNs with different morphologies (PANI-R-900 and PANI-T-900). The SEM micrographs depicted in Figure 1 of PANI-R and PANI-T samples clearly show two very distinct morphologies. In Figure 1a, the SEM images of PANI-R taken at different magnifications show the near granular shape of the nanoparticles, with a mean diameter of aggregated particles of approximately 150 nm. SEM images of PANI-R-900 (Figure 1b) indicate that the general morphological features are preserved after carbonization, with a sizable decrease in grain size. Figure 1c highlights the nanofiber morphology of the PANI-T sample with a rough surface of nanofibers, which are interconnected in bunch-like structures. In this case, the approximate mean diameter of nanofibers is around 130 nm, but some thicker rods may be observed because of the agglomeration of nanofibers. The carbonization process caused almost negligible changes in the morphology of PANI-T (Figure 1d); nonetheless, the PANI-T-900 sample presented a relatively smooth surface of nanofibers compared with PANI-T.
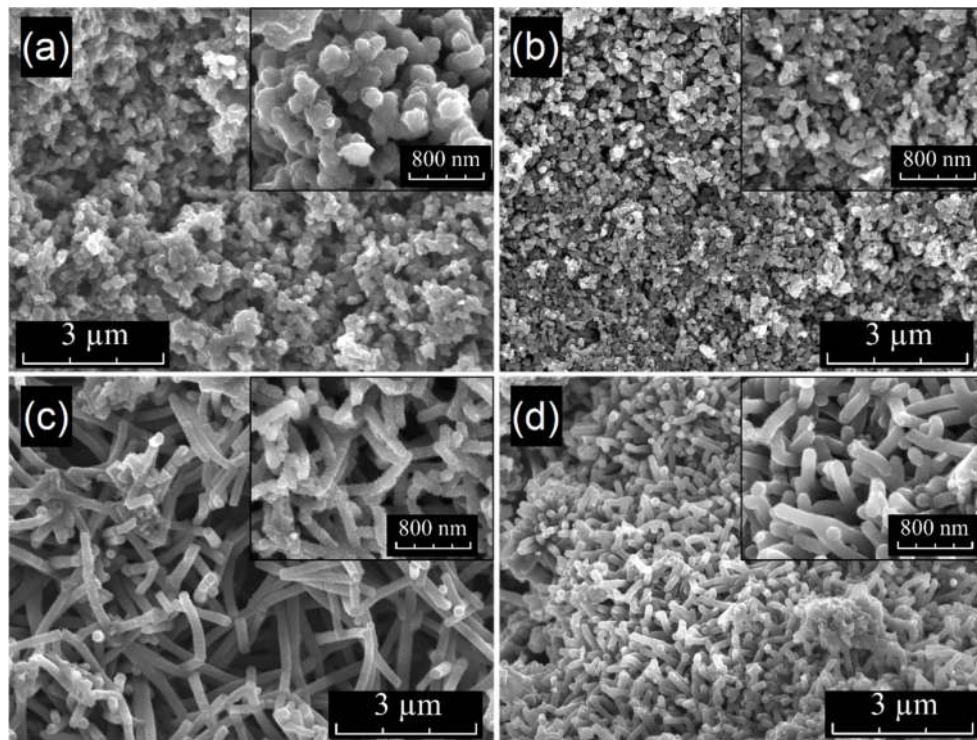
Figure 1. SEM images of (**a**) PANI-R (scale bar 3 μm), (**b**) PANI-R-900 (scale bar 3 μm), (**c**) PANI-T (scale bar 3 μm), and (**d**) PANI-T-900 (scale bar 3 μm). The insets present SEM images acquired at higher magnification with a scale bar of 800 nm.

From energy dispersive X-ray analysis (EDX), the elemental compositions of all samples are summarized in Table 1, and the original data of all samples are presented in the Supplementary Materials (Figures S1–S4), which indicate the presence of C, N, O, and S atoms for PANI-R and PANI-T, with a higher at % of N and O in the case of PANI-R. The N content in PANI-R is close to its theoretical content calculated upon the chemical

structure of the aniline unit as the atomic C:N ratio is 6 and is higher in the case of PANI-T. After carbonization of PANI-R and PANI-T, the EDX analysis (Table 1) indicates the presence of C, N and O atoms in both samples with an increased contribution of the carbon content and a significant drop in at % of oxygen, which is a common characteristic given by the carbonization process of the polymer precursors. Furthermore, the results show that a significant amount of nitrogen is preserved in the samples after carbonization, highlighting the high stability of the N-doped carbon nanostructures, which can enhance the conductivity and hydrophilicity of the graphitic network. The EDS mapping of PANI-R-900 and PANI-T-900 show that the N and O are homogeneously distributed in the graphitic network for both carbonized samples (Figure S5).

Table 1. Elemental composition of the materials from EDX.

Sample	C (at %)	N (at %)	O (at %)	S (at %)
PANI-R	73.34	10.99	12.92	2.74
PANI-T	82.08	8.08	6.20	3.64
PANI-R-900	89.95	6.49	3.56	NA
PANI-T-900	92.42	5.02	2.56	NA

NA—not available.

Thus, in our work, we synthesized polyaniline with different morphologies, which was further used as a polymeric precursor for NCNs. The results prove that the direct carbonization of polyaniline nanostructures is an easy and economical process to obtain nitrogen-rich carbon materials, preserving the general features of the precursor's morphology, with a smaller decrease in nanoparticle size, as can be seen in the SEM images and EDX analysis of the polymer precursors and their corresponding NCNs.

2.1.2. FT-IR Spectroscopy

In Figure 2, the FT-IR spectra of PANI-R and PANI-T are shown, along with their corresponding NCNs. The characteristic peaks of PANI-R (Figure 2a) appearing around ~1583 cm^{-1} and ~1493 cm^{-1} are assigned to the C=C stretching vibration of the quinoid and benzenoid rings, respectively. The band at ~1306 cm^{-1} can be attributed to the C–N–C stretching vibration or to the π-electron delocalization induced in the polymer through protonation, while the band at 1248 cm^{-1} is attributed to the C–N$^{+•}$ stretching mode of the polaron structure, which is characteristic of the conducting protonated form of PANI [34–36]. The band around 1144 cm^{-1} can be assigned to a C-H bending vibration or the vibrations of the charged polymer units Q=NH^{+}–B or B–NH$^{+•}$–B (Q denotes the quinoid ring and B denotes the benzenoid ring), formed during protonation [34,35,37].

The bands at about 1080 cm^{-1} and 700 cm^{-1} correspond to hydrogen sulfate counterions, which are characteristic of the conducting form of PANI [35]. The bands appearing between 880 cm^{-1}–800 cm^{-1} are attributed to the aromatic C–H vibrations. In addition to the above peaks, the spectrum of the PANI-R exhibits bands at 3238 cm^{-1} that are attributed to N-H stretching mode, and the absorption between ~3063 cm^{-1}–2830 cm^{-1} corresponds to an aromatic C–H stretching vibration [34,37,38]. In comparison with the spectrum of PANI-R, the spectrum of PANI-T (Figure 2b) contains new additional bands positioned at 1448 cm^{-1}, 1042 cm^{-1}, 750 cm^{-1} and 688 cm^{-1}, which can be associated with the different morphology of the samples, as reported previously [35]. Thus, the band at 1448 cm^{-1} corresponds to the skeletal C=C stretching vibration of the aromatic ring; 1042 cm^{-1} is due to the sulphonate groups attached to the aromatic rings [39]. The bands observed at 750 cm^{-1} and 688 cm^{-1} are related to the monosubstituted aromatic rings as terminal units or indicate more pronounced branching chains in the nanofiber samples [35,39,40].

The FTIR spectra of both carbonized samples show almost no peaks in the whole range of 400–4000 cm^{-1}, except for the two broad bands with maxima at 1580 cm^{-1} and 1132 cm^{-1}. The first one is assigned to the aromatic ring vibration mixed with C=N

stretching vibration, and the second ones correspond to C–C and C–N vibrations, respectively. These bands are characteristic of carbon-like materials that have Raman G- and D-bands, which are not IR active. The presence of nitrogen in our carbonized samples, also confirmed by the EDX analysis, breaks the symmetry of the carbon network, and these bands become active in the FTIR spectra [41–43].
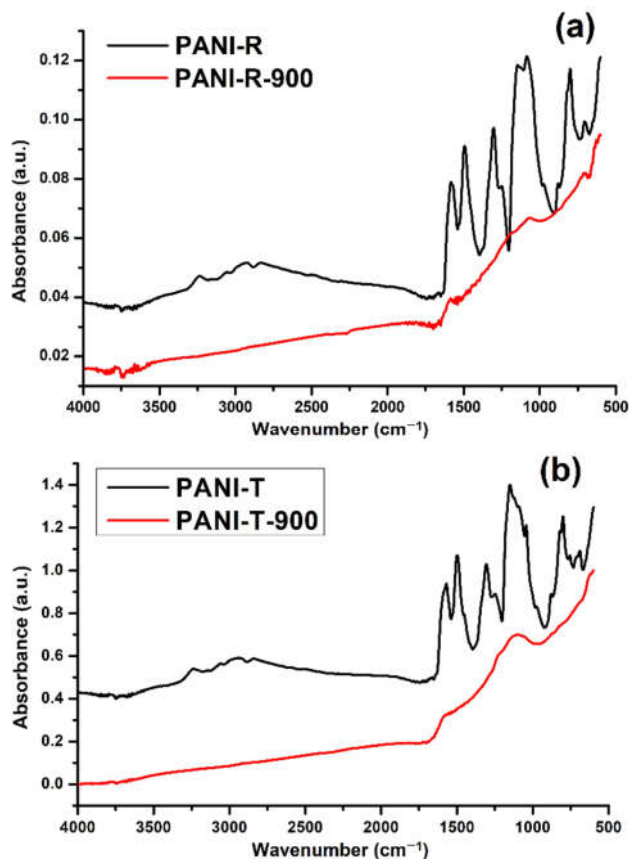

Figure 2. FTIR spectra of (**a**) PANI-R and PANI-R-900 and (**b**) PANI-T and PANI-T-900 samples.

2.1.3. X-ray Diffraction

The X-ray diffraction patterns from Figure 3 present the structural characterization of both polymers and the NCNs obtained after thermal treatment of polymers. In Figure 3a, the XRD analyses of PANI-R and PANI-T show two broad peaks at 2θ values of 20.2° and 25.5°, assigned to the parallel and perpendicular periodicity to the polyaniline chain's direction, respectively [44,45], which indicates the amorphous phase of samples. Notably, the XRD scattering pattern of the PANI-T highlights better-defined peaks, indicating the formation of a more ordered structure compared to PANI-R. This may be due to the inter-chain hydrogen bonding or electrostatic interaction between adjacent polymer chains caused by differences in morphology and preparation method [44,46,47]. Based on these results, the morphology of the polymer materials can influence the crystallinity of the sample, as reported in the literature [45]. Moreover, Figure 3b,c shows the XRD profiles of PANI-R and PANI-T samples after the thermal treatment performed in an N_2 atmosphere at a temperature of 900 °C (PANI-R-900 and PANI-T-900, respectively). The carbonization of PANI-R and PANI-T is highlighted by the presence of two broad peaks corresponding to diffraction planes (002) and (101) of a disordered graphite phase [48]. To obtain quantitative information on the microstructural features, the Rietveld analysis was performed on experimental data using the Diffraction (MAUD) program [49]. For both

samples, the crystalline coherence length and microstrain were obtained after Rietveld refinement of structural parameters. In sample PANI-R-900, the value of the crystallite size is 3.7 ± 0.6 nm, which is very similar to PANI-T-900, which was 3.8 ± 0.7 nm. Further, the microstrain has a slightly different value for PANI-R-900, $1.1 \times 10^{-1} \pm 2.4 \times 10^{-3}$, in comparison with $9.6 \times 10^{-2} \pm 2.1 \times 10^{-3}$ for PANI-T-900. These sensitive differences in microstructural parameters between the two samples also show that the nanofiber morphology of PANI-T, which has a better periodicity of polymer chains, favored the formation of a more ordered graphite phase than the sample PANI-R.
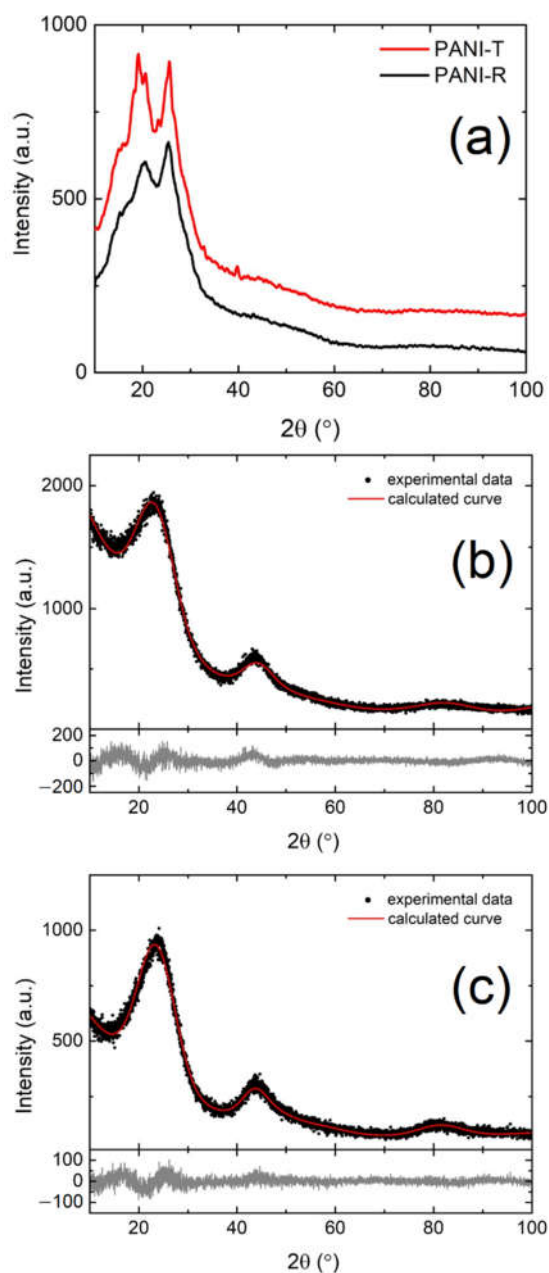

Figure 3. (**a**) XRD patterns of PANI-R and PANI-T; XRD experimental data and Rietveld refinement with residuals at the graphs bottom of (**b**) PANI-R-900 and (**c**) PANI-T-900.

2.2. Performance of MFCs with NCN-Modified Anodes

In our study, 1 kΩ external resistance was used for anode biofilm inoculation. For the polarization measurements, the optimal resistance, defined as the external resistance for producing maximum power in MFCs, or a high external resistance (1 kΩ), which can facilitate a more compact structure of the biofilm, can be used [50,51]. As reported, it is important to have a mature anode biofilm with stable performance, and for an MFC with an H-type configuration, the operational voltage becomes stable 15 days after inoculation, or in less time if a mixed-culture anode is used [50]. In our case, the voltage became stable after 145 h for the MFCs using the PANI-T-900-modified anode and 200 h for MFCs using the PANI-R-900-modified anode. The polarization measurements confirm that both modifications of carbon cloth with PANI-R-900 and PANI-T-900 as MFC anodes showed an ability for electricity generation. The power density and polarization curves generated in MFCs are shown in Figure 4. The maximum power densities were affected by the NCN used for anode modification, being well recognized that the nature of modifier materials influences the performance of MFCs [7–9]. As can be seen in Figure 4, the maximum power density of 40.4 mW/m^2 is obtained in the case of anode modification with NCNs with nanofibrillar morphology, PANI-T-900, compared with 32.3 mW/m^2 obtained for anode modification with PANI-R-900 and 18.8 mW/m^2 for MFC with carbon cloth (CC) anode. The average values (four replicas for each modification) of open circuit potential (OCP), power and current density and internal resistance for MFC, which used the same modifier for the MFC anode, PANI-R-900 and PANI-T-900, are summarized in Table 2.
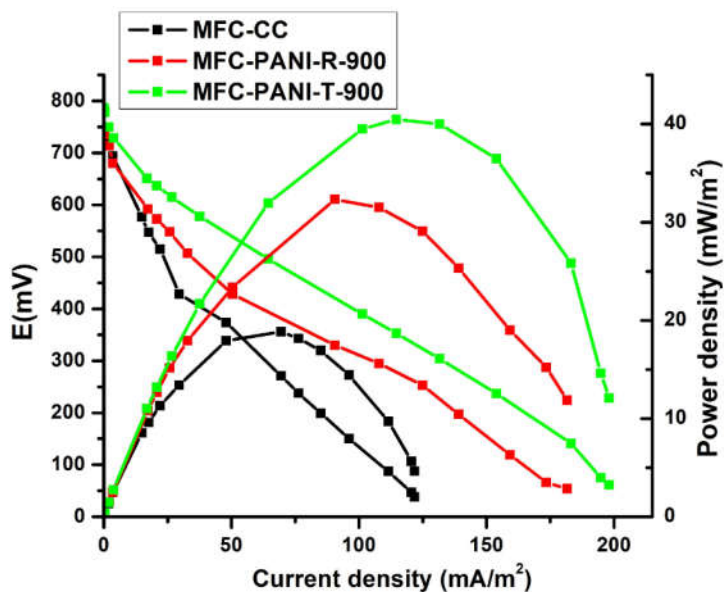
Figure 4. Polarization and power density curves of MFC with CC and PANI-R-900- and PANI-T-900-modified anodes.

Table 2. Average values of open circuit potential (OCP), power and current density and internal resistance of MFC modified with PANI-R-900 and PANI-T-900 and MFC with CC anode.

MFC Index	OCP (mV)	P (mW/m^2)	R_{int} (Ω)
MFC-CC	702.5 ± 24.5	15.2 ± 2.6	1437.6 ± 122.6
MFC-PANI-R-900	761.2 ± 28.7	30.6 ± 1.9	875.2 ± 52.9
MFC-PANI-T-900	789.7 ± 31.3	38.5 ± 1.9	808.7 ± 48.6

The polarization measurements show that the internal resistance of the cell followed the order: CC (1272 Ω) > PANI-R-900-modified CC anode (839 Ω) > PANI-T-900-modified

CC anode (782 Ω) (see Table S1). According to the results obtained, the anode modification with PANI-T-900 is considered to be more beneficial for the improvement of MFC performance in terms of power generation. The nanofibrillar morphology of PANI-T-900, with both its larger specific surface area, given by the well-defined individual NCNs separated by microgaps and micropores, and higher conductivity, due to a better periodicity of polymer chains, which is also preserved in the carbonised samples, can facilitate better bacterial colonization and more efficient substrate transport [52]. Based on the NCN characterizations, the NCN with the nanofibrillar morphology provides a better organization of the carbon network, which implies a higher conductivity and a small content oxygen content in the carbon network that may improve the performance of the MFC [53,54]. Moreover, the fiber shapes can accelerate both direct and indirect electron transfer to optimize the MFC output [54]. As a consequence, the better performance of the MFC with the modified PANI-T-900 anode may be associated with the nanofibrillar morphology of NCNs.

2.3. Biofilm Characterization

The microbial community formed on the surface of the PANI-R-900- and PANI-T-900-modified CC anodes, as well as the microbial community of the initial wastewater, were characterized through metabarcoding techniques. The V_3V_4 region of the bacterial 16S rRNA gene from the total biofilm DNA samples was amplified and sequenced using NGS (Illumina, San Diego, CA, USA) technologies.

Results show that the operating conditions as well as the anode type determined an enrichment of select taxa from the initial wastewater. Regarding alpha-diversity metrics (Table 3), there was an increase in both Shannon entropy and Faith's phylogenetic distance (Faith's PD) from the initial wastewater to the anode biofilms. The PANI-R-900-modified anode had the highest Shannon diversity of all sample types, indicating the greatest variation in feature relative abundance. Faith's PD increased significantly ($p < 0.05$) in the anode biofilms from the initial wastewater. Pielou's evenness values did not differ greatly, although a slight decrease was observed in the case of the PANI-T-900-modified anodes, indicating a larger variation within more closely related taxa when compared to the PANI-R-900-modified anodes.

Table 3. Alpha diversity across sample types. Shannon entropy, Pielou's evenness, and Faith's phylogenetic distance were calculated using qiime2 core metrics phylogenetic.

Sample Type	Shannon	Faith's Phylogenetic Distance	Pielou's Evenness
Initial Wastewater	11.33 ± 0.28	322.26 ± 176.34	0.9407 ± 0.0027
PANI-R-900	12.16 ± 0.13	835.92 ± 86.04	0.9408 ± 0.0042
PANI-T-900	11.92 ± 0.12	811.30 ± 24.31	0.9294 ± 0.0049

Feature taxonomy at the class level underwent major changes when comparing the most abundant taxa from the initial wastewater to the anode biofilms (Figure 5). The initial wastewater had a community consisting of mainly Campylobacteria, of which the main constituents were *Arcobacter* sp. (22.9%), *Pseudoarcobacter* sp. (14.81%), and unclassified *Arcobacteraceae* (17.83%), the family being one of the most abundant in raw sewage and wastewater samples [55]. Other abundant classes were *Gammaproteobacteria* (19.19%) and *Bacteroidia* (16.22%), also commonly present in wastewater [56].

In the anode biofilms, *Campylobacteria* and *Gammaproteobacteria* relative abundance decreased greatly, while *Bacteroidia* abundance increased, more so in the case of PANI-T-modified anodes, 28.22% compared to 23.9% for PANI-R-900. The most enriched classes for both anode types were *Thermoanaerobacteria* (PANI-T-900—16.12%; PANI-R-900—13.73%), *Desulfuromonadia* (PANI-T-900—11.73%; PANI-R-900—8.42%), *Clostridia* (greater abundance in PANI-R, 9.99%, and 6.88% in PANI-T), *Synergistia*, *Desulfobacteria* and *Desulfovibrionia*.
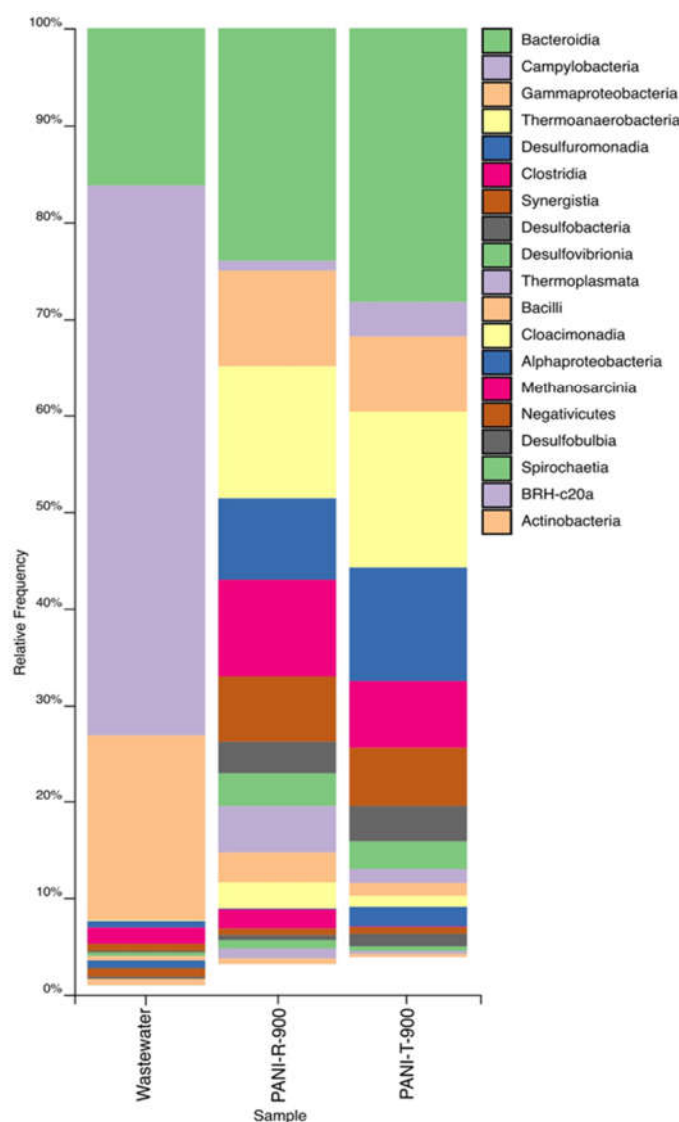
Figure 5. Barplot representation of most abundant classes across the three sample types. Relative frequencies represent the mean-ceiling of triplicate datasets.

Taxa classified by the SILVA database as belonging to the *Thermoanaerobacteria* class are more commonly classified into *Clostridia*, the only genus present being *Thermoanaerobacter* (Figure 6). Species belonging to this genus have been observed as dominant in other MFC systems and also used in pure culture form for electrical current generation, colonizing the system anodes [57,58]. *Desulfuromonadia*, *Desulfobacteria* and *Desulfovibrionia* are members of the *Desulfobacterota* phylum, whose members are characterized by their dissimilatory sulphate reduction capability [59], a trait relevant to the bioremediation component of MFC functionality. *Synergistia* includes bacteria commonly associated with acetate metabolism [60], and its presence could be justified by the addition of the initial wastewater through acetate addition. Although the air present in the anodic chamber was not removed through special procedures, the main taxa forming the biofilm on the MFC anodes are obligate anaerobes, indicating that throughout the MFC operation period, oxygen was depleted, allowing the enrichment of these bacterial classes. Additionally, the greater abundance of anaerobic taxa in the biofilm of the PANI-T-900-modified CC anode could be due to the decreased oxygen content of the nanofibrillar structures.
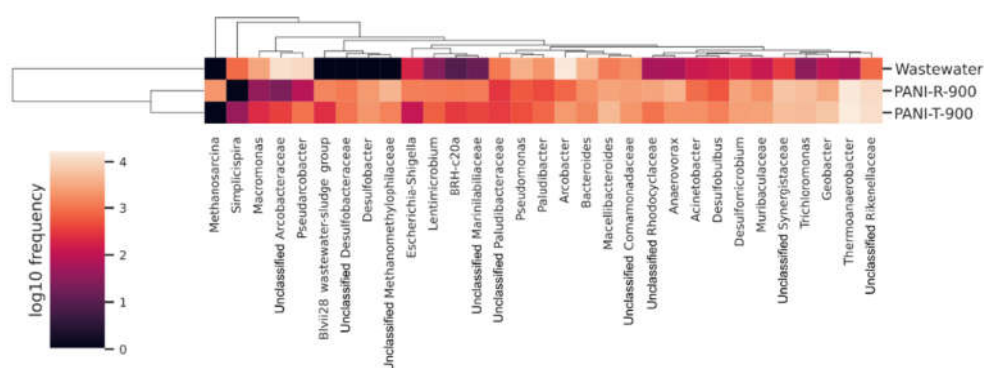
Figure 6. Heatmap representation of genera of at least 1% relative abundance, log normalized. Samples and features were clustered based on Bray-Curtis distances. Relative frequencies represent the mean-ceiling of triplicate datasets.

MFC operation determined an enrichment of *Archaea*, from an abundance of 0.035% in the initial wastewater to 7.26% and 1.77% in the PANI-R- and PANI-T-modified CC anodes, respectively. The presence of *Archaea*, namely *Methanosarcinales* (class *Halobacterota*, 1.96% in PANI-R-900) and *Methanomassilicoccales* (class *Thermoplasmata*, 4.79%—PANI-R-900, 1.44%—PANI-T-900), a characteristic of anaerobic systems, could bring added value to the MFC system through methanogenesis from acetate [56].

At the genus and family levels (Figure 6), results show multiple taxa with high relative abundance, which are frequently associated with the ability for extracellular electron transfer (EET). The *Geobacter* genus, the type genus studied for its exoelectrogenic capabilities [61,62], had a relative abundance more than twofold greater in the case of the PANI-T-900-modified CC anode (6.62%) than the PANI-R-900-modified CC anode (3.05%), representing a possible justification for its better power generation. Furthermore, *Thermoanaerobacter* sp. (as mentioned previously) and *Macellibacteroides* [63] were more abundant in the PANI-T-900 CC biofilm, possibly contributing to MFC performance.

Other known EET-capable bacterial taxa enriched in the case of both anode modifiers used are *Trichloromonas* [64] and members of the *Rhodocyclaceae* and *Comamonadaceae* families [65].

3. Materials and Methods

3.1. Synthesis of Nitrogen-Containing Carbon Nanostructures

Direct carbonization of polyaniline (PANI) as an N-containing aromatic polymer with N covalently bonded in polymeric precursors is an efficient way to prepare N-containing carbon nanostructures, most frequently by preserving the morphology of the PANI precursor.

Two different synthesis methods were used to obtain different morphologies for PANI precursors. In the first method, polyaniline nanostructures were prepared by the chemical oxidative polymerization of an aniline monomer in acid media using ammonium persulfate as the oxidizing agent, following a modified procedure of an adapted method previously reported by Rezvani et al. [66]. In a typical reaction, 0.1 M aniline was dissolved in 0.1 M H_2SO_4 under stirring conditions at room temperature for 30 min. A total of 0.1 M ammonium persulfate was dissolved in 50 mL of 0.1 M H_2SO_4 and pre-cooled before adding to the monomer solution drop by drop. The polymerization solution was allowed to react overnight at room temperature. The resulting precipitate was collected and washed several times with deionized water and methanol. Finally, the product was dried at 60 °C overnight and indexed as PANI-R. The second procedure for the synthesis of polyaniline nanostructures was carried out using a template-free self-assembly method in an appropriate mixed solution of 0.4 M ethanol and 0.4 M acetic acid, as reported in

reference [67]. Separately, 1.82 mL of aniline monomer was dissolved in 100 mL of the mixed solution, and 5.71 g of ammonium peroxydisulfate was dissolved in 100 mL of the mixed solution. The solutions of aniline and oxidant were cooled at a temperature between 0–5 °C for 30 min and then mixed rapidly into a beaker while being stirred vigorously for 30 s. The mixture was left to react overnight at ~0–5 °C, and then the product was filtered and washed with deionized water and methanol and finally dried at 50–60 °C in an oven overnight at ambient conditions. The final product was indexed as PANI-T.

NCNs were obtained after carbonization of PANI-R and PANI-T at 900 °C under nitrogen flow, with a 5 °C/min heating rate and 1 h holding time at 900 °C, followed by free cooling to room temperature under nitrogen flow. The NCN samples were indexed as PANI-R-900 and PANI-T-900, respectively.

3.2. Material Characterization

The morphological characteristics and elemental composition of PANI nanostructures and corresponding NCNs were analyzed using scanning electron microscopy (Tescan MAIA-3 field-emission electron microscope (TESCAN, Brno, Czech Republic), using a secondary electron detector and 5 kV accelerating voltage), coupled with an energy dispersive X-ray spectrometer (EDX QUANTAX 200 X-Flash 6/30, from Bruker, Billerica, MA, USA). Quantification of the EDX spectra was performed using the Kα lines by means of the Bruker ESPRIT Quant v2.3 software.

Fourier transform infrared (FTIR) spectroscopy analysis of the PANI nanostructure samples was performed by recording 128 scans in the range of 600–4000 cm^{-1}, with a resolution of 4 cm^{-1} on a Varian 3100 Excalibur spectrophotometer (Varian, Palo Alto, CA, USA). The samples were analyzed by attenuated total reflection (ATR) using a Pike MIRacle (Ge crystal) accessory. The crystalline features of PANI nanostructures and corresponding NCNs were characterized by X-ray diffraction (XRD) using a Bruker D8 Discover diffractometer (CuKα = 1.54 Å) in symmetric geometry. The data were collected in the interval of 2θ =10–80° with an angular step of 0.02° at ambient conditions.

3.3. Microbial Fuel Cell Design and Operation

The double chamber is commonly used in laboratory research for the investigation of new substrates, electrode materials, membranes or types of microbial communities, and it is known for its low power generation because of its complex design and high internal resistance [7,68]. A double chamber MFC with an H-type configuration (Figure S6), made of glass and separated by a Nafion 117 Proton Exchange Membrane (PEM), was used to test the performance of the anode modified with NCNs. Anodes were made of non-wet proofed carbon cloth (CC) modified with NCNs and connected to the external circuits containing a 1 kΩ resistor using titanium wire and crocodile clips. For the anode modification, a suspension of NCNs (1 mg/mL) in ethanol aqueous solution (1:1 *v/v*) containing 0.5% Nafion was prepared. After homogenization in an ultrasonic bath for 30 min, the ink was sprayed onto the carbon cloth surface using an airbrush. The loading of NCNs on carbon cloth for all MFCs was ~1.1 mg/cm^2. For Pt-containing cathodes, commercial Pt catalyst (40 wt% Pt/C, Alfa Aesar, Haverhill, MA, USA) ink mixed with a chemical binder (5% Nafion solution) was sprayed over carbon cloth. The anolyte consisted of municipal wastewater (S.C. Distributie Apa si Canalizare Magurele SRL, Ilfov Romania) supplemented with 1 g/L of acetate, and phosphate buffer (0.05 M, pH 7.0 ±0.01) was used as the catholyte. The anode chamber was hermetically sealed, while the cathode chamber was purged with bubbling air. Cell voltages across the external resistor were recorded using a Pico Data Logger ADC-24 (Pico Technology, Cambridgeshire, UK) and a personal computer. For each modification, four identical MFCs with PANI-R-900- and PANI-T-900-modified CC anodes were operated simultaneously and compared with MFC using a CC anode as a controller. The polarization curves and power output were obtained by varying the external resistor from 1 MΩ to 40 Ω. The open cell potential (OCP) was measured after 120 min. At each resistance, MFC ran for at least 10 min to ensure that a stable power

output had been achieved. Current (I) was calculated as I = V (cell voltage)/R (external resistance), and power (P) was calculated as P = I × V. Both current density and power density were calculated based on the surface area of the anode.

3.4. Biofilm Sample Collection and DNA Extraction. Sequence and Statistical Analysis

Anode biofilm and initial wastewater total DNA were isolated using the Dneasy PowerSoil Kit (#12888; Qiagen, Hilden, Germany) according to the manufacturer's protocol, including the additional incubation step at 70 °C before vortexing samples. DNA, RNA, and protein quantification were done using a Qubit 4.0 and the dsDNA BR (#Q32850; Thermo Fisher Scientific, Waltham, MA, USA), RNA HS (#Q32852, Thermo Fisher Scientific), and Protein (#33211, Thermo Fisher Scientific) Assay Kits. Triplicate samples were selected for each anode type (PANI-R-900; PANI-T-900) and initial wastewater based on quality and DNA concentration. Sequencing was externalized towards Novogene (https://en.novogene.com/, accessed on 15 march 2022). Samples were amplified using universal primers for the V_3-V_4 region of the bacterial 16S rRNA gene (sequencing depth—100 k tags). The PCR products were selected by 2% agarose gel electrophoresis (Agilent 5400, Agilent, Santa Clara, CA, USA). Equal amounts of PCR product from each sample were pooled, end-repaired, A-tailed, and further ligated with Illumina adapters. Libraries were sequenced on a paired-end Illumina platform to generate 250 bp paired-end raw reads. Data analysis was performed in-house using the QIIME2 toolkit [69]. Sequencing data were denoised and quality-controlled using DADA2 [70]. SEPP [71] was used for the phylogenetic placement of ASVs into a reference tree based on the SILVA 128 database [72]. A classifier based on the SILVA 138 99% database was used, together with the q2-feature-classifier (classify-sklearn) plugin [73], for the taxonomical annotation of ASVs.

4. Conclusions

In this paper, polyaniline with different morphologies was used as a precursor for the synthesis of nitrogen-containing carbon nanostructures. The NCNs with different morphology were considered for anode modification, and the resulting MFC performance was studied and compared with MFC with carbon cloth anode as controls. The maximum power density of 40.4 mW/m² was obtained in the case of anode modification with PANI-T-900, which has a nanofibrillar morphology, being 1.25 times higher when compared to the anode modified with PANI-R-900 and 2.15 times higher than the MFC using the CC anode. The internal resistance reduction also resulted in the improvement of power generation. MFC operation determined the enrichment of various taxa, resulting in community profiles that differed greatly from the initial wastewater. The dominant taxa in the anode biofilms were part of genera and families associated with extracellular electron transfer, such as *Geobacter*, *Thermoanaerobacter*, *Rhodocyclaceae*, and *Comamonadaceae*. The use of PANI-T-900-modified CC anodes resulted in greater relative abundances for members of *Geobacter* and *Thermoanaerobacter*, justifying the MFCs' better power generation. The majority of taxa identified were anaerobic, while bacteria from the *Desulfobacterota* phylum indicated the occurrence of sulphate reduction. The presence of methanogenic *Archaea* in the biofilms could indicate the synthesis of methane, a possible value-added byproduct, throughout the process. Since the experimental results proved that both modifications with NCNs lead to a better performance of MFCs, polyaniline-derived nitrogen-containing carbon nanostructures can be considered a very good material for MFC anode modification, especially due to the simple and economical process that can allow the introduction of nitrogen functionality on the anode surface. Further research would be necessary to undertake in order to correlate the change in nitrogen functionality with NCN morphology.

Supplementary Materials: The following supporting information can be downloaded at: www.mdpi.com/1422-0067/231/91/1230/s1.

References

1. Dwivedi, K.A.; Huang, S.-J.; Wang, C.-T.; Kumar, S. Fundamental Understanding of Microbial Fuel Cell Technology: Recent Development and Challenges. *Chemosphere* **2022**, *288*, 132446.
2. Pandit, S.; Savla, N.; Sonawane, J.M.; Sani, A.M.; Gupta, P.K.; Mathuriya, A.S.; Rai, A.K.; Jadhav, D.A.; Jung, S.P.; Prasad, R. Agricultural Waste and Wastewater as Feedstock for Bioelectricity Generation Using Microbial Fuel Cells: Recent Advances. *Fermentation* **2021**, *7*, 169. https://doi.org/10.3390/fermentation7030169.
3. Savla, N.; Pandit, S.; Khanna, N.; Mathuriya, A.S.; Jung, S.P. Microbially Powered Electrochemical Systems Coupled with Membrane-Based Technology for Sustainable Desalinization and Efficient Wastewater Treatment. *J. Korean Soc. Environ. Eng.* **2020**, *42*, 360–380.
4. Pawar, A.A.; Karthic, A.; Lee, S.; Pandit, S.; Jung, S.P. Microbial Electrolysis Cells for Electromethanogenesis: Materials, Configurations and Operations. *Environ. Eng. Res.* **2020**, *27*, 200484.
5. Zahid, M.; Savla, N.; Pandit, S.; Thakur, V.K.; Jung, S.P.; Gupta, P.K.; Prasad, R.; Marsili, E. Microbial Desalination Cell: Desalination through Conserving Energy. *Desalination* **2022**, *521*, 115381.
6. Kang, H.; Kim, E.; Jung, S.P. Influence of Flowrates to a Reverse Electro-Dialysis (RED) Stack on Performance and Electrochemistry of a Microbial Reverse Electrodialysis Cell (MRC). *Int. J. Hydrogen Energy* **2017**, *42*, 27685–27692.
7. Obileke, K.; Onyeaka, H.; Meyer, E.L.; Nwokolo, N. Microbial Fuel Cells, a Renewable Energy Technology for Bio-Electricity Generation: A Mini-Review. *Electrochem. Commun.* **2021**, *125*, 107003.
8. Greenman, J.; Gajda, I.; You, J.; Mendis, B.A.; Obata, O.; Pasternak, G.; Ieropoulos, I. Microbial Fuel Cells and Their Electrified Biofilms. *Biofilm* **2021**, *3*, 100057.
9. Dumitru, A.; Scott, K. Anode Materials for Microbial Fuel Cells. In *Microbial Electrochemical and Fuel Cells*; Elsevier: Amsterdam, The Netherlands, 2016; pp. 117–152, ISBN 9781782423751.
10. Jung, S.-H.; Ahn, Y.-H.; Oh, S.-E.; Lee, J.-H.; Cho, K.-T.; Kim, Y.-J.; Kim, M.-W.; Shim, J.-M.; Kang, M.-S. Impedance and Thermodynamic Analysis of Bioanode, Abiotic Anode, and Riboflavin-Amended Anode in Microbial Fuel Cells. *Bull. Korean Chem. Soc.* **2012**, *33*, 3349–3354.
11. Nam, T.; Son, S.; Koo, B.; Hoa Tran, H.V.; Kim, J.R.; Choi, Y.; Jung, S.P. Comparative Evaluation of Performance and Electrochemistry of Microbial Fuel Cells with Different Anode Structures and Materials. *Int. J. Hydrogen Energy* **2017**, *42*, 27677–27684.
12. Kang, H.; Jeong, J.; Gupta, P.L.; Jung, S.P. Effects of Brush-Anode Configurations on Performance and Electrochemistry of Microbial Fuel Cells. *Int. J. Hydrogen Energy* **2017**, *42*, 27693–27700.
13. Yaqoob, A.A.; Ibrahim, M.N.M.; Rodríguez-Couto, S. Development and Modification of Materials to Build Cost-Effective Anodes for Microbial Fuel Cells (MFCs): An Overview. *Biochem. Eng. J.* **2020**, *164*, 107779.
14. Sonawane, J.M.; Yadav, A.; Ghosh, P.C.; Adeloju, S.B. Recent Advances in the Development and Utilization of Modern Anode Materials for High Performance Microbial Fuel Cells. *Biosens. Bioelectron.* **2017**, *90*, 558–576.

15. Baro, M.; Jaidev; Ramaprabhu, S. Conductive and Nitrogen-Enriched Porous Carbon Nanostructure Derived from Poly (Para-Phenylenediamine) for Energy Conversion and Storage Applications. *Appl. Surf. Sci.* **2020**, *503*, 144069.

16. Yu, Y.-Y.; Guo, C.X.; Yong, Y.-C.; Li, C.M.; Song, H. Nitrogen Doped Carbon Nanoparticles Enhanced Extracellular Electron Transfer for High-Performance Microbial Fuel Cells Anode. *Chemosphere* **2015**, *140*, 26–33.

17. Zhu, K.; Wang, S.; Liu, H.; Liu, S.; Zhang, J.; Yuan, J.; Fu, W.; Dang, W.; Xu, Y.; Yang, X.; et al. Heteroatom-Doped Porous Carbon Nanoparticle-Decorated Carbon Cloth (HPCN/CC) as Efficient Anode Electrode for Microbial Fuel Cells (MFCs). *J. Clean. Prod.* **2022**, *336*, 130374.

18. Wu, X.; Qiao, Y.; Guo, C.; Shi, Z.; Li, C.M. Nitrogen Doping to Atomically Match Reaction Sites in Microbial Fuel Cells. *Commun. Chem.* **2020**, *3*, 68. https://doi.org/10.1038/s42004-020-0316-z.

19. Haider, M.R.; Jiang, W.-L.; Han, J.-L.; Sharif, H.M.A.; Ding, Y.-C.; Cheng, H.-Y.; Wang, A.-J. In-Situ Electrode Fabrication from Polyaniline Derived N-Doped Carbon Nanofibers for Metal-Free Electro-Fenton Degradation of Organic Contaminants. *Appl. Catal. B* **2019**, *256*, 117774.

20. Wang, X.; He, Z.; Shi, Y.; Li, B. Nitrogen-Doped Ordered Mesoporous Carbon as Metal-Free Catalyst for Power Generation in Single Chamber Microbial Fuel Cells. *J. Electrochem. Soc.* **2017**, *164*, F620–F627.

21. Ci, S.; Wen, Z.; Chen, J.; He, Z. Decorating Anode with Bamboo-like Nitrogen-Doped Carbon Nanotubes for Microbial Fuel Cells. *Electrochem. Commun.* **2012**, *14*, 71–74.

22. Liu, Y.; Jin, X.-J.; Tuo, A.-X.; Liu, H. Improved Oxygen Reduction Reaction Activity of Three-Dimensional Porous N-Doped Graphene from a Soft-Template Synthesis Strategy in Microbial Fuel Cells. *RSC Adv.* **2016**, *6*, 105211–105221.

23. Xing, X.; Liu, Z.; Chen, W.; Lou, X.; Li, Y.; Liao, Q. Self-Nitrogen-Doped Carbon Nanosheets Modification of Anodes for Improving Microbial Fuel Cells' Performance. *Catalysts* **2020**, *10*, 381.

24. Guan, Y.-F.; Zhang, F.; Huang, B.-C.; Yu, H.-Q. Enhancing Electricity Generation of Microbial Fuel Cell for Wastewater Treatment Using Nitrogen-Doped Carbon Dots-Supported Carbon Paper Anode. *J. Clean. Prod.* **2019**, *229*, 412–419.

25. Qian, X.; Zhang, F.; Zhao, Y.; Liang, K.; Luo, W.; Yang, J. Polydopamine-Derived Carbon: What a Critical Role for Lithium Storage? *Front. Energy Res.* **2020**, *8*, 140. https://doi.org/10.3389/fenrg.2020.00140.

26. Stejskal, J.; Kohl, M.; Trchová, M.; Kolská, Z.; Pekárek, M.; Křivka, I.; Prokeš, J. Conversion of Conducting Polypyrrole Nanostructures to Nitrogen-Containing Carbons and Its Impact on the Adsorption of Organic Dye. *Mater. Adv.* **2021**, *2*, 706–717.

27. Song, Y.; Qin, Z.; Huang, Z.; Liu, T.; Li, Y.; Liu, X.-X. Nitrogen-Doped Carbon "Spider Webs" Derived from Pyrolysis of Polyaniline Nanofibers in Ammonia for Capacitive Energy Storage. *J. Mater. Res.* **2018**, *33*, 1109–1119.

28. Iftimie, S.; Bradu, C.; Dumitru, A. Carbon Nanotubes and Carbonized Polyaniline Nanostructures as 3D Modified Anode for Microbial Fuel Cells. *Proc. Rom. Acad.* **2019**, *20*, 45–50.

29. Kang, Z.; Jiao, K.; Xu, X.; Peng, R.; Jiao, S.; Hu, Z. Graphene Oxide-Supported Carbon Nanofiber-like Network Derived from Polyaniline: A Novel Composite for Enhanced Glucose Oxidase Bioelectrode Performance. *Biosens. Bioelectron.* **2017**, *96*, 367–372.

30. Kang, Z.; Jiao, K.; Cheng, J.; Peng, R.; Jiao, S.; Hu, Z. A Novel Three-Dimensional Carbonized PANI1600@CNTs Network for Enhanced Enzymatic Biofuel Cell. *Biosens. Bioelectron.* **2018**, *101*, 60–65.

31. Yuan, H.; Dong, G.; Li, D.; Deng, L.; Cheng, P.; Chen, Y. Steamed Cake-Derived 3D Carbon Foam with Surface Anchored Carbon Nanoparticles as Freestanding Anodes for High-Performance Microbial Fuel Cells. *Sci. Total Environ.* **2018**, *636*, 1081–1088.

32. Gezginci, M.; Uysal, Y. The Effect of Different Substrate Sources Used in Microbial Fuel Cells on Microbial Community. *JSM Environ. Sci. Ecol.* **2016**, *4*, 1035.

33. Zhang, L.; Shen, Z.; Fang, W.; Gao, G. Composition of Bacterial Communities in Municipal Wastewater Treatment Plant. *Sci. Total Environ.* **2019**, *689*, 1181–1191.

34. Shao, W.; Jamal, R.; Xu, F.; Ubul, A.; Abdiryim, T. The Effect of a Small Amount of Water on the Structure and Electrochemical Properties of Solid-State Synthesized Polyaniline. *Materials* **2012**, *5*, 1811–1825.

35. Trchová, M.; Stejskal, J. Polyaniline: The Infrared Spectroscopy of Conducting Polymer Nanotubes (IUPAC Technical Report). *Pure Appl. Chem.* **2011**, *83*, 1803–1817.

36. Dutta, S.; Manna, K.; Srivastava, S.K.; Gupta, A.K.; Yadav, M.K. Hollow Polyaniline Microsphere/Fe_3O_4 Nanocomposite as an Effective Adsorbent for Removal of Arsenic from Water. *Sci. Rep.* **2020**, *10*, 4982.

37. Ibrahim, K.A. Synthesis and Characterization of Polyaniline and Poly(Aniline-Co-o-Nitroaniline) Using Vibrational Spectroscopy. *Arab. J. Chem.* **2017**, *10*, S2668–S2674.

38. Husin, M.R.; Arsad, A.; Suradi, S.S.; Alothman, O.; Ngadi, N.; Kamaruddin, M.J. Fourier Transforms Infrared Spectroscopy and X-Ray Diffraction Investigation of Recycled Polypropylene/Polyaniline Blends. *Chem. Eng. Trans.* **2017**, *56*, 1015–1020.

39. Tang, S.-J.; Wang, A.-T.; Lin, S.-Y.; Huang, K.-Y.; Yang, C.-C.; Yeh, J.-M.; Chiu, K.-C. Polymerization of Aniline under Various Concentrations of APS and HCl. *Polym. J.* **2011**, *43*, 667–675.

40. Trchová, M.; Seděnková, I.; Konyushenko, E.N.; Stejskal, J.; Holler, P.; Ćirić-Marjanović, G. Evolution of Polyaniline Nanotubes: The Oxidation of Aniline in Water. *J. Phys. Chem. B* **2006**, *110*, 9461–9468.

41. Janošević, A.; Pašti, I.; Gavrilov, N.; Mentus, S.; Krstić, J.; Mitrić, M.; Travas-Sejdic, J.; Ćirić-Marjanović, G. Microporous Conducting Carbonized Polyaniline Nanorods: Synthesis, Characterization and Electrocatalytic Properties. *Microporous Mesoporous Mater.* **2012**, *152*, 50–57.

42. Mentus, S.; Ćirić-Marjanović, G.; Trchová, M.; Stejskal, J. Conducting Carbonized Polyaniline Nanotubes. *Nanotechnology* **2009**, *20*, 245601.

43. Rozlívková, Z.; Trchová, M.; Exnerová, M.; Stejskal, J. The Carbonization of Granular Polyaniline to Produce Nitrogen-Containing Carbon. *Synth. Met.* **2011**, *161*, 1122–1129.
44. Mazzeu, M.A.C.; Faria, L.K.; Cardoso, A.D.M.; Gama, A.M.; Baldan, M.R.; Gonçalves, E.S. Structural and Morphological Characteristics of Polyaniline Synthesized in Pilot Scale. *J. Aerosp. Technol. Manag.* **2017**, *9*, 39–47.
45. Wang, J.; Wang, J.; Yang, Z.; Wang, Z.; Zhang, F.; Wang, S. A Novel Strategy for the Synthesis of Polyaniline Nanostructures with Controlled Morphology. *React. Funct. Polym.* **2008**, *68*, 1435–1440.
46. Bhadra, S.; Khastgir, D. Determination of Crystal Structure of Polyaniline and Substituted Polyanilines through Powder X-Ray Diffraction Analysis. *Polym. Test.* **2008**, *27*, 851–857.
47. Chaudhari, H.K.; Kelkar, D.S. X-Ray Diffraction Study of Doped Polyaniline. *J. Appl. Polym. Sci.* **1996**, *62*, 15–18.
48. Vlahov, A. XRD Graphitization Degrees: A Review of the Published Data and New Calculations, Correlations, and Applications. *Geol. Balk.* **2021**, *50*, 11–35.
49. Lutterotti, L.; Bortolotti, M.; Ischia, G.; Lonardelli, I.; Wenk, H.-R. Rietveld Texture Analysis from Diffraction Images. *Z. Krist.* **2007**, *2007*, 125–130.
50. Tran, H.V.; Kim, E.; Jung, S.P. Anode Biofilm Maturation Time, Stable Cell Performance Time, and Time-Course Electrochemistry in a Single-Chamber Microbial Fuel Cell with a Brush-Anode. *J. Ind. Eng. Chem.* **2022**, *106*, 269–278.
51. Koo, B.; Lee, S.-M.; Oh, S.-E.; Kim, E.J.; Hwang, Y.; Seo, D.; Kim, J.Y.; Kahng, Y.H.; Lee, Y.W.; Chung, S.-Y.; et al. Addition of Reduced Graphene Oxide to an Activated-Carbon Cathode Increases Electrical Power Generation of a Microbial Fuel Cell by Enhancing Cathodic Performance. *Electrochim. Acta* **2019**, *297*, 613–622.
52. Zhou, H.; Chen, H.; Luo, S.; Lu, G.; Wei, W.; Kuang, Y. The Effect of the Polyaniline Morphology on the Performance of Polyaniline Supercapacitors. *J. Solid State Electrochem.* **2005**, *9*, 574–580.
53. Fan, X.; Zhou, Y.; Jin, X.; Song, R.-B.; Li, Z.; Zhang, Q. Carbon Material-based Anodes in the Microbial Fuel Cells. *Carbon Energy* **2021**, *3*, 449–472.
54. Choudhury, P.; Prasad Uday, U.S.; Bandyopadhyay, T.K.; Ray, R.N.; Bhunia, B. Performance Improvement of Microbial Fuel Cell (MFC) Using Suitable Electrode and Bioengineered Organisms: A Review. *Bioengineered* **2017**, *8*, 471–487.
55. Venâncio, I.; Luís, Â.; Domingues, F.; Oleastro, M.; Pereira, L.; Ferreira, S. The Prevalence of Arcobacteraceae in Aquatic Environments: A Systematic Review and Meta-Analysis. *Pathogens* **2022**, *11*, 244. https://doi.org/10.3390/pathogens11020244.
56. Ferrera, I.; Sánchez, O. Insights into Microbial Diversity in Wastewater Treatment Systems: How Far Have We Come? *Biotechnol. Adv.* **2016**, *34*, 790–802.
57. Lusk, B.G.; Colin, A.; Parameswaran, P.; Rittmann, B.E.; Torres, C.I. Simultaneous Fermentation of Cellulose and Current Production with an Enriched Mixed Culture of Thermophilic Bacteria in a Microbial Electrolysis Cell. *Microb. Biotechnol.* **2018**, *11*, 63–73.
58. Lusk, B.G.; Khan, Q.F.; Parameswaran, P.; Hameed, A.; Ali, N.; Rittmann, B.E.; Torres, C.I. Characterization of Electrical Current-Generation Capabilities from Thermophilic Bacterium *Thermoanaerobacter pseudethanolicus* Using Xylose, Glucose, Cellobiose, or Acetate with Fixed Anode Potentials. *Environ. Sci. Technol.* **2015**, *49*, 14725–14731.
59. Waite, D.W.; Chuvochina, M.; Pelikan, C.; Parks, D.H.; Yilmaz, P.; Wagner, M.; Loy, A.; Naganuma, T.; Nakai, R.; Whitman, W.B.; et al. Proposal to Reclassify the Proteobacterial Classes Deltaproteobacteria and Oligoflexia, and the Phylum Thermodesulfobacteria into Four Phyla Reflecting Major Functional Capabilities. *Int. J. Syst. Evol. Microbiol.* **2020**, *70*, 5972–6016.
60. Zhu, X.; Campanaro, S.; Treu, L.; Kougias, P.G.; Angelidaki, I. Novel Ecological Insights and Functional Roles during Anaerobic Digestion of Saccharides Unveiled by Genome-Centric Metagenomics. *Water Res.* **2019**, *151*, 271–279.
61. Poddar, S.; Khurana, S. Geobacter: The Electric Microbe! Efficient Microbial Fuel Cells to Generate Clean, Cheap Electricity. *Indian J. Microbiol.* **2011**, *51*, 240.
62. Hu, Y.; Wang, Y.; Han, X.; Shan, Y.; Li, F.; Shi, L. Biofilm Biology and Engineering of *Geobacter* and *Shewanella* spp. for Energy Applications. *Front. Bioeng. Biotechnol.* **2021**, *9*, 786416.
63. Patel, D.; Bapodra, S.L.; Madamwar, D.; Desai, C. Electroactive Bacterial Community Augmentation Enhances the Performance of a Pilot Scale Constructed Wetland Microbial Fuel Cell for Treatment of Textile Dye Wastewater. *Bioresour. Technol.* **2021**, *332*, 125088.
64. Liu, H.-Z.; Zhang, Y.; Yang, S.-X.; Wang, N.; Liu, H.-B.; Li, J.-C. Introducing Electrolysis to Enhance Anaerobic Digestion Resistance to Acidification. *Bioprocess Biosyst. Eng.* **2022**, *45*, 515–525.
65. Jangir, Y.; French, S.; Momper, L.M.; Moser, D.P.; Amend, J.P.; El-Naggar, M.Y. Isolation and Characterization of Electrochemically Active Subsurface *Delftia* and *Azonexus* Species. *Front. Microbiol.* **2016**, *7*, 756.
66. Rezvani, M.; Asgharinezhad, A.A.; Ebrahimzadeh, H.; Shekari, N. A Polyaniline-Magnetite Nanocomposite as an Anion Exchange Sorbent for Solid-Phase Extraction of Chromium(VI) Ions. *Mikrochim. Acta* **2014**, *181*, 1887–1895.
67. Huang, Z.; Liu, E.; Shen, H.; Xiang, X.; Tian, Y.; Xiao, C.; Mao, Z. Preparation of Polyaniline Nanotubes by a Template-Free Self-Assembly Method. *Mater. Lett.* **2011**, *65*, 2015–2018.
68. Jung, S.; Regan, J.M. Comparison of Anode Bacterial Communities and Performance in Microbial Fuel Cells with Different Electron Donors. *Appl. Microbiol. Biotechnol.* **2007**, *77*, 393–402.
69. Bolyen, E.; Rideout, J.R.; Dillon, M.R.; Bokulich, N.A.; Abnet, C.C.; Al-Ghalith, G.A.; Alexander, H.; Alm, E.J.; Arumugam, M.; Asnicar, F.; et al. Reproducible, Interactive, Scalable and Extensible Microbiome Data Science Using QIIME 2. *Nat. Biotechnol.* **2019**, *37*, 852–857.

70. Callahan, B.J.; McMurdie, P.J.; Rosen, M.J.; Han, A.W.; Johnson, A.J.A.; Holmes, S.P. DADA2: High-Resolution Sample Inference from Illumina Amplicon Data. *Nat. Methods* **2016**, *13*, 581–583.

71. Mirarab, S.; Nguyen, N.; Warnow, T. SEPP: SATé-Enabled Phylogenetic Placement. In Proceedings of the Pacific Symposium on Biocomputing, Kohala Coast, HI, USA, 3–7 January 2012; pp. 247–258.

72. Quast, C.; Pruesse, E.; Yilmaz, P.; Gerken, J.; Schweer, T.; Yarza, P.; Peplies, J.; Glöckner, F.O. The SILVA Ribosomal RNA Gene Database Project: Improved Data Processing and Web-Based Tools. *Nucleic Acids Res.* **2012**, *41*, D590–D596.

73. Bokulich, N.A.; Kaehler, B.D.; Rideout, J.R.; Dillon, M.; Bolyen, E.; Knight, R.; Huttley, G.A.; Gregory Caporaso, J. Optimizing Taxonomic Classification of Marker-Gene Amplicon Sequences with QIIME 2's Q2-Feature-Classifier Plugin. *Microbiome* **2018**, *6*, 90. https://doi.org/10.1186/S40168-018-0470-Z.